Soft Matter

Acoustic trap-and-release for rapid assessment of cell motility

Journal:	*Soft Matter*
Manuscript ID	SM-ART-01-2019-000184.R1
Article Type:	Paper
Date Submitted by the Author:	26-Mar-2019

Complete List of Authors:	Kim, Minji; Washington University in Saint Louis, Mechanical Engineering & Materials Science Huff, Emma; Washington University in Saint Louis, Biomedical Engineering Bottier, Mathieu; Washington University in Saint Louis, Mechanical Engineering & Materials Science; Washington University in Saint Louis School of Medicine, Genetics Dutcher, Susan; Washington University in Saint Louis School of Medicine, Genetics Bayly, Philip; Washington University in Saint Louis, Mechanical Engineering & Materials Science Meacham, J. Mark; Washington University in Saint Louis, Mechanical Engineering & Materials Science

Soft Matter

ARTICLE

Acoustic trap-and-release for rapid assessment of cell motility†

Minji Kim,[a] Emma Huff,[b] Mathieu Bottier,[a,c] Susan K. Dutcher,[c] Philip V. Bayly,[a] and J. Mark Meacham*[a]

Received 00th January 20xx,
Accepted 00th January 20xx

DOI: 10.1039/x0xx00000x

www.rsc.org/

Functional cilia and flagella are crucial to the propulsion of physiological fluids, motile cells, and microorganisms. Motility assessment of individual cells allows discrimination of normal from dysfunctional behavior, but cell-scale analysis of individual trajectories to represent a population is laborious and impractical for clinical, industrial, and even research applications. We introduce an assay that quantifies swimming capability as a function of the variation in polar moment of inertia of cells released from an acoustic trap. Acoustic confinement eliminates the need to trace discrete trajectories and enables automated analysis of hundreds of cells in minutes. The approach closely approximates the average speed estimated from the mean squared displacement of individual cells for wild-type *Chlamydomonas reinhardtii* and two mutants (*ida3* and *oda5*) that display aberrant swimming behaviors. Large-population acoustic trap-and-release rapidly differentiates these cell types based on intrinsic motility, which provides a highly sensitive and efficient alternative to conventional particle tracing.

Introduction

In ciliated cells that line human airways, oviduct, and ependyma of the brain, the coordinated beating of hairlike cilia propels fluid in specific directions. Cilia dysfunction disrupts these critical flows. In swimming cells and unicellular organisms (e.g., spermatozoa, algae, protists), abnormal motion of the cilia alters propulsive efficacy. In humans, defects in ciliary structure and function are implicated in several cilia-related disorders (ciliopathies), including primary ciliary dyskinesia (PCD), infertility, chronic otitis media, and hydrocephalus.[1-5] Nanometer-scale electron microscopy and high-resolution (sub-micron in space and millisecond in time) optical microscopy of individual cilia/flagella have allowed researchers to connect specific structural defects to atypical waveforms, diminished propulsive efficacy, and impaired movement.[6-11] Complementary measures of cell motility (e.g., swimming speed and propulsive power) provide a more direct comparison of normal and aberrant cell behavior.[10-13] Quantitative motility assessment at the cell level requires imaging and analysis of *individual cell* trajectories.[12-17] These micron- to millimeter-scale investigations of cell motion are less demanding than imaging cilia/flagella waveforms at sub-micron scales, but characterization of individual cells remains laborious, and many measurements are needed to accurately represent a given population. Alternatively, methods that agglomerate cells based on their attraction to (or repulsion from) a physical stimulus like light (phototaxis) or gravity (gravitaxis) can discriminate *cell populations* with normal and inhibited motility; however, these global measurements often lack sufficient sensitivity to distinguish partial inhibition from complete loss of motility.[18] In this work, we introduce a rapid assay that achieves the efficiency of extant population-based approaches while maintaining the sensitivity of individual-based assessments to evaluate the motility of a population of microorganisms released from a two-dimensional (2D) standing bulk acoustic wave (SBAW) trap. Acoustic confinement concentrates cells in a tight agglomerate irrespective of an inherent taxis, which allows exquisite control over the predefined (and narrow) region of interest for subsequent automatable analysis.

The well-established swimming characteristics of individual wild-type and mutant *Chlamydomonas reinhardtii* cells provide the motility variation needed to evaluate the proposed method. This biflagellate, unicellular alga provides a biochemical and genetic model for studying ciliary function and assembly. The ultrastructure of the *C. reinhardtii* flagellum (the "9+2" axoneme) comprises a radial array of nine microtubule doublets connected to each other by the nexin-dynein regulatory complex, and a central pair complex that is connected transiently by radial spokes.[19] Mechanical properties and the activity of dynein motor proteins determine the dynamic behavior of the flagellum. Thus, the integrity of these structural and functional components is critical to cell motility. The 9+2 axonemal structure is conserved in human cilia; hence, *C. reinhardtii* is invaluable in the study of ciliopathies.[20-23]

[a] *Department of Mechanical Engineering and Materials Science, Washington University in St. Louis, St. Louis, Missouri 63130, USA; E-mail: meachamjm@wustl.edu; Tel: +1 (314) 935-3821*
[b] *Department of Biomedical Engineering, Washington University in St. Louis, St. Louis, Missouri 63130, USA*
[c] *Department of Genetics, Washington University School of Medicine in St. Louis, St. Louis, Missouri 63110, USA*

† Electronic Supplementary Information (ESI) available: Text describes the relationship of ΔJ/CSA to MSD in an ideal case and the practical implementation; movie files demonstrate low population release and swimming assessment, and the large-population trap-and-release comparison of swimming for the three *C. reinhardtii* strains studied here. See DOI: 10.1039/x0xx00000x

Furthermore, laboratory culture and genetic modification are straightforward, which facilitates the examination of ciliary defects. A large catalog of *C. reinhardtii* mutants that exhibit clear differences in swimming effectiveness are available for testing changes in ciliary movement and motility.

Here, we exploit *C. reinhardtii* to establish the utility of acoustic trap-and-release as a cell motility assay. We first confirm that a standing acoustic field of sufficient strength to form a tight cell agglomerate of various mutants does not damage cells or affect flagellar function. The method is then used to discriminate wild-type and mutant cells by calculating their swimming speeds in two ways, which are based on mean squared displacement (MSD) determined from individual cell trajectories and the variation in the polar area moment of inertia, ΔJ, of spreading cell populations. For each cell type, these average speeds are found to be nearly identical to each other and to closely approximate intrinsic swimming speeds reported in the literature.[7, 9, 15, 24-26] Acoustic trap-and-release measurements accurately represent the altered motility of the two mutants and, importantly, clearly identify differences in their swimming capability. Finally, we extend the analysis to demonstrate determination of swimming speeds for large populations, assessing hundreds of cells automatically and in a matter of minutes.

Materials and methods

Finite Element Analysis Predictive Modeling

Piezoelectric materials and transducer thicknesses were selected for operation in the 0.5 to 2.5-MHz range. The Acoustics module of COMSOL Multiphysics[27] was used to select the size of a circular microfluidic chamber that would support eigenshapes (pressure fields) capable of trapping cell populations at eigenfrequencies of ~1 MHz. Two-dimensional (2D) eigenanalyses included only the fluid domain, and the suspension medium was approximated as water (density ρ_w = 998 kg/m^3; speed of sound c_w = 1481 m/s). Glass channel walls were modelled using the sound hard boundary condition. The simple model provided qualitative evidence that millimeter-scale (in diameter) circular chambers would support mode shapes suitable for trap-and-release experiments. For example, the mode shape predicted for a 3.0-mm diameter chamber driven at 1.34 MHz exhibited a strong central node in which swimming cells might become acoustically-confined (see overlaid model pressure field in Fig. 2a; red and blue contours represent total pressure maxima and minima, respectively, with a zero-pressure nodal region at the center of the chamber). Because isotropic wet etching causes lateral expansion of patterned features (and a corresponding shift to lower resonant frequencies; see Fabrication, Assembly, and Operation of the Acoustic Trap), the experimental actuation frequency was expected to reside below the model-predicted operating point. Thus, the actual chamber resonance was identified by sweeping the transducer actuation frequency over a 200-kHz range below the model-predicted resonance.

Fabrication, Assembly, and Operation of the Acoustic Trap

A 60-µm deep, 3.1-mm diameter chamber was isotropically etched into a 1.5-mm thick soda lime/chromium blank precoated with positive photoresist (5300 Å AZ1500, Telic Co.) as described previously.[28] A solution of 49% (w/w) HF:69% (w/w) HNO_3:deionized (DI) water at a ratio of 2:1:6 was used to isotropically etch patterned features to a depth of ~60 µm. Isotropic expansion resulted in an actual chamber diameter of ~3.1 mm; however, resultant deviation from the predicted harmonic response did not preclude identification of an operating frequency (see below). The chamber was enclosed using calcium-assisted bonding to a second blank with predrilled 1-mm diameter inlet and outlet holes.[29] Briefly, the two blanks were rinsed with a 0.5% Alconox, 0.5% (w/v) calcium(II) acetate hydrate (Sigma-Aldrich) slurry in DI water. After a subsequent wash in DI water, the two surfaces were brought together and placed in an oven at 115°C for two hours to drive off excess water. After dicing to size, the final microfluidic chip dimensions were 63 mm × 36 mm × 3 mm.

The experimental assembly consisted of a 24 mm × 28 mm × 0.75 mm PZT-8 piezoelectric transducer (APC 880, American Piezo Ceramics) clamped to the top side of the microfluidic chip using water as an acoustic coupling medium. Although the effectiveness of an acoustofluidic device (i.e., the ability to focus and trap microparticles at a particular fluidic channel or chamber resonance) is dependent on transducer placement,[30, 31] our experience with similar bulk acoustic wave (BAW)-based devices[28] indicates that the present configuration is able to excite desired resonances. Examples described in the literature also report that lateral resonances can be created perpendicular to the direction of transmission of the piezoelectric transducer.[32, 33] After loading the chamber with cells, the trapping frequency was found by sweeping the transducer actuation over a 200-kHz range (5-kHz increment) that included the predicted resonance of interest (33522A, Agilent; 2100L, ENI). The modal analysis neglected the influence of the actuator/resonator and did not account for the inherent three-dimensionality of isotropically-etched features. Thus, it is unsurprising that the experimentally-determined resonance of 1.15 MHz was somewhat below the predicted value. When driven at the identified resonance, suspended cells formed a tight agglomerate at the chamber center. Having confirmed the device operating parameters, the piezoelectric transducer was epoxied to the top of the glass chip. The operating frequency (f = 1.15 MHz) was consistent for all cell types and concentrations. The operating voltage was 43.5 V.

Selection of *Chlamydomonas reinhardtii* Strains

Three strains of biflagellate *Chlamydomonas reinhardtii* were used in this study. Wild-type cells (strain CC-125) were used as a baseline for *C. reinhardtii* swimming. The inner dynein arm (IDA) mutant *ida3* (CC-2668) and the outer dynein arm (ODA) mutant *oda5* (CC-2236) were chosen because they exhibit swimming characteristics that are distinctly different from CC-125 and each other. Mutant strains were generated from meiotic crosses.[34] Cell size was uniform for each cell type, and

the cell diameters [7.2±0.8 μm for CC-125 ($n_{CC\text{-}125}$ = 30), 6.2±0.9 μm for *ida3* (n_{ida3} = 30), and 7.3±0.9 μm for *oda5* (n_{oda5} = 18)] were well-suited to acoustic trapping in the low-MHz frequency range.

Cell Culture and Sample Preparation

CC-125, *ida3*, and *oda5* cells were obtained from the Dutcher Lab at Washington University in St. Louis. Cells were grown on agar plates at 25°C under constant lighting following a previously-reported protocol.[35] Three hours prior to a trap-and-release experiment, cells were resuspended in a test tube containing medium that lacked nitrogen to promote gametogenesis. Growth medium was adapted from Medium I of Sager and Granick.[36] Test tubes were vortexed to create a uniform suspension for chamber loading. For low-population studies, cells were prepared at a concentration of ~2×10^6 cells/mL. A concentration of ~5×10^6 cells/mL was used for large-population studies. Concentrations were confirmed by manual count after fixing cells with glutaraldehyde (Sigma-Aldrich). *C. reinhardtii* cells are mesophilic and grow best at moderate temperatures ranging from 20 to 32°C.[37] To maintain high cell viability while ensuring consistent and repeatable results, experiments were performed on a temperature-controlled microscope stage insert (PE100, Linkam) at 20°C.

The microfluidic chamber was pretreated with 0.5% (w/v) bovine serum albumin (BSA) (Sigma-Aldrich) in phosphate-buffered saline to minimize adhesion of cells to the glass channel walls. The chamber was stored at 4°C when not in use to prevent BSA denaturation. The glass chip was equilibrated to room temperature before loading cells.

Video Microscopy

Visualization of *C. reinhardtii* trap-and-release was performed on the stage of an inverted microscope (Axio Observer z.1, Zeiss) using a 10X objective (EC Plan-Neofluar 10x/0.30 M27, Zeiss). Videos were recorded at 38.15 frames per second (fps) at 1932×1460-pixel resolution (0.454 μm × 0.454 μm/pixel) using a 3-Megapixel camera and imaging software (Axiocam 503; ZEN software, Zeiss). Between each experimental condition, the microfluidic chamber was flushed with DI water and inspected under the microscope to ensure that no cells from the previous experiment remained.

Image Processing and Analysis

Brightfield images were cropped to an appropriate window size (300 μm × 300 μm for low-population studies and 500 μm × 500 μm for large-population studies) centered around the cell aggregate. For MSD calculation, each cell trajectory in a low-population experiment was traced manually using the Manual Tracking plugin in ImageJ.[38] Automatic particle tracing failed to correctly detect cell trajectories when cells were condensed at the center of the acoustic trap. The microfluidic chamber depth (60 μm) was larger than the cell diameter (~10 μm), allowing cells to overlap and further complicating use of automatic tracing. Manual tracing allowed visual identification of the initial segment of each trajectory (including z-position). For ΔJ/CSA determination, brightfield images were first converted into binary images in ImageJ. The Slice Geometry feature of the BoneJ plugin[39] was used to calculate the cross-sectional area (CSA) and second moment of area of the regions occupied by black pixels. MATLAB[40] was used to identify the centroid of a composite of these regions and to determine the change in its polar moment of inertia, ΔJ (see ΔJ/CSA Closely Approximates MSD for Radial Cell Spreading and Electronic Supplementary Information for mathematical development). Average speeds, U, were determined by fitting U^2t^2 to MSD and the ratio ΔJ/CSA using the lsqcurvefit function in MATLAB. For low-population studies, curve fits and s.d. bands were weighted by contributing sample sizes ($N_{CC\text{-}125}$ = 3, $n_{g,CC\text{-}125}$ = 13, 20, 9; N_{ida3} = 3, $n_{g,ida3}$ = 21, 14, 9; N_{oda5} = 3, $n_{g,oda5}$ = 16, 9, 9), i.e., MSD- and ΔJ/CSA-based speeds were determined for each individual release experiment, and a weighted average was used to determine the speeds representative of each cell type. For large population studies, the sample concentration (~5×10^6 cells/mL) dictated the approximate cell count per trap (~50); however, individual cell counts were not recorded. Thus, curve fits and s.d. bands were not weighted by sample size, i.e., ΔJ/CSA-based speed was determined by a simple average across six release experiments.

Effect of Acoustic Trap-and-Release on Cell Swimming and Viability

Repeat trap-and-release experiments were used to assess the effects of ultrasound exposure on the swimming behavior and viability of *C. reinhardtii* cells. Five consecutive trap-and-release cycles were performed at 75-second intervals on the same cell populations. Cells were not replaced during the experiment and were monitored for damage presenting as decreased motility (i.e., spread speed). The sequence of trap-and-release cycles was repeated four times (n = 4).

Results and Discussion

Acoustic Field-Particle Interactions Allow for Size-Selective Immobilization

The nature of interactions between an acoustic field and suspended particles enables manipulation and trapping of the *C. reinhardtii* cell body without restricting the oscillatory motion of the flagella. The acoustic radiation force arising from the scattering of acoustic waves on a particle is predominant for microscale objects in the low-MHz frequency range.[41, 42] Thus, the cell body (~10-μm diameter) is well-suited to generation of large trapping forces, while the nanoscale flagella (~200-nm diameter cross-section) should be only weakly affected. Acoustic manipulation of cells is contact- and label-free,[43-47] and biological cells are found to remain viable even after prolonged exposure to an ultrasound field.[48-51] Based on previous work, viscosity, heat conduction, and multi-particle effects can be neglected for low MHz-frequency actuation of dilute suspensions of particles with radius, a, larger than ~3 μm.[52, 53] Further, many studies have shown that to a first approximation cells behave as compressible spheres with positive acoustic contrast factors (i.e., cells move to zero-pressure nodal regions

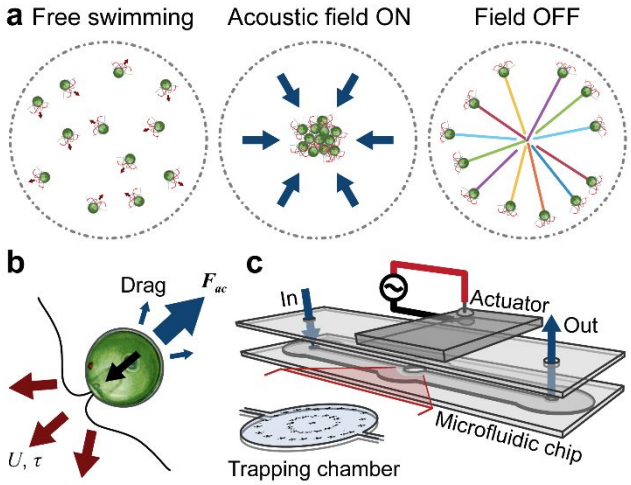

Fig. 1. Acoustic trap-and-release concept and device schematic. (a) A standing acoustic field is used to first trap (field on) and then release (field off) freely swimming cells for subsequent analysis. (b) The balance of swimming strength (U, τ), the acoustic radiation force ($\boldsymbol{F}_{ac}$), and drag govern motion of individual cells suspended in a standing acoustic pressure field. (c) Schematic illustrating a device assembly and circular trapping chamber geometry suitable for trapping cells at a single location.

when suspended in an ultrasonic standing wave field).[46, 52, 54, 55] Although flagellated cells deviate from ideal sphericity, the trapping phenomenon is explained by introducing the acoustic radiation force, $\boldsymbol{F}_{ac}$, on a small, compressible spherical particle in an inviscid fluid, i.e.,[56-60]

$$\boldsymbol{F}_{ac} = -\frac{4\pi}{3}a^3\nabla\left[f_1\frac{1}{2}\kappa_o\langle p_{in}^2\rangle - f_2\frac{3}{4}\rho_o\langle v_{in}^2\rangle\right], \quad (1)$$

where

$$f_1 = 1-\tilde{\kappa} \text{ and } f_2 = \frac{2(\tilde{\rho}-1)}{2\tilde{\rho}+1}. \quad (2)$$

Here, p_{in} and v_{in} are the incoming acoustic pressure and velocity fields at the particle location, and $\langle\ \rangle$ denotes a time average over a full oscillation period of a time-harmonic quantity; f_1 and f_2 are dimensionless functions of the ratios of particle (sub p) to medium (sub o) density and compressibility, $\tilde{\rho} = \rho_p/\rho_o$ and $\tilde{\kappa} = \kappa_p/\kappa_o$. Thus, acoustic confinement is a complex function of field parameters (amplitude and frequency), size, and the material properties of the cells and suspension medium. Further, the degree to which a population contracts within a pressure well depends on the intrinsic swimming strength of a given cell type. In the experiments reported here, actuation amplitude was scaled to produce similarly sized aggregates of wild-type and mutant populations.

Ultrasound Standing Waves Confine Motile *C. reinhardtii* Cells without Affecting Cell Function

The acoustic trap-and-release concept and device schematic are illustrated in Fig. 1. The motion of individual cells suspended in a microfluidic trapping chamber is governed by the balance of swimming strength, the acoustic radiation force (Eq. 1), and drag (see Fig. 1b). To form a cell aggregate at a single point, an ideal standing acoustic pressure field must exhibit a circularly symmetric pressure node. Finite element analysis (FEA) modeling was used to select a circular chamber with eigenfrequencies/eigenmodes suitable for cell trapping at ~1 MHz. The resultant 3.1-mm diameter, trapping chamber was isotropically etched into glass to a depth of 60 µm and enclosed using a second glass capping layer. A bulk piezoelectric transducer was used to actuate the assembled device at identified chamber resonant frequencies.

The glass microfluidic device was used to assess the ability of the acoustic trap-and-release method to discriminate swimming of three strains of biflagellate *C. reinhardtii* [wild-type cells (strain CC-125) and two mutants, strains *ida3* (CC-2668) and *oda5* (CC-2236)]. Nutrient-deficient medium promoted gametogenesis to yield populations of actively swimming cells with a uniform size distribution. After loading the trapping chamber with cells, the unimpeded random motion of freely swimming cells formed a uniform distribution within the chamber. When driven at resonant frequencies of the chamber, a standing wave field instantaneously developed, and cells became confined to pressure minima (nodes) of the acoustic field (Fig. 2a).

The transducer actuation frequency was swept over a 200-kHz range (5-kHz increment) about a model-predicted chamber resonance until maximum contraction of the central cell aggregate was observed (see Fig. 2a; overlaid contours of the model pressure field are included in Fig. 2a for reference). At a chamber resonant frequency of 1.15 MHz, a strong central

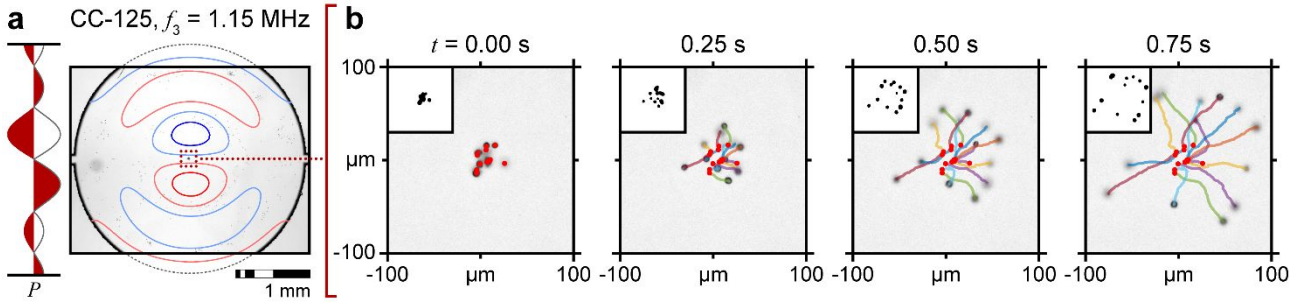

Fig. 2. Acoustic trap-and-release implementation. (a) Glass microfluidic chamber loaded with swimming wild-type (strain CC-125) *C. reinhardtii* cells and acoustically excited at a chamber resonance with a circularly symmetric central pressure node. (b) Release of contracted CC-125 agglomerate. Particle tracing and binary images (insets) are used to determine MSD and ΔJ/CSA, respectively, for the ballistic swimming regime.

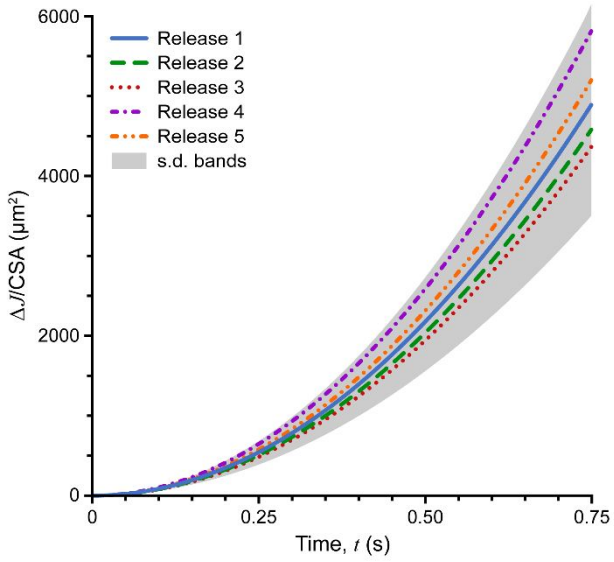

Fig. 3. Repeated acoustic trap-and-release effect on cell swimming and viability. Comparison of U^2t^2 as functions of ΔJ/CSA-based speeds for each of five consecutive release cycles on the same populations of wild-type (CC-125) C. reinhardtii cells (data represent n = 4 sequences on four populations). The gray region represents the range from the lower s.d. of ΔJ/CSA = U^2t^2 for Release 3 to the upper s.d. for Release 4.

pressure well formed a compact agglomerate for all cell types. Strongly swimming cells were able to enter and exit weaker concentric nodal regions near the chamber periphery; however, no cells joined or left the central population that was analyzed. Importantly, no change in the swimming behavior of *C. reinhardtii* was observed after repeated ultrasound exposure during sequential trap-and-release of the same population. Average spread speeds for CC-125 cells were 91.4±8.7, 91.2±16.2, 87.0±9.8, 101.1±3.1, and 97.3±6.7 μm/s for subsequent release cycles, indicating that repeated exposure to an ultrasound acoustic field does not affect cell motility/ intrinsic speed or viability (see Fig. 3).

C. reinhardtii Behaves as a Ballistic Swimmer on Short Time Scales

On relatively long time scales, *C. reinhardtii* swimming behavior is described as a random walk; cell movement alternates between straight swimming and random reorientation.[61, 62] However, in the initial time before cells make a first turn, the mean squared displacement of an individual cell is simply expressed as MSD = U^2t^2 where U is the cell speed and t is the time.[61-63] We define this time period as the ballistic regime during which cells follow a relatively straight path at constant velocity. At any given time, each cell in the trap has a random orientation. When the acoustic field is turned off, cells maintain their pre-release orientations and freely swim outward from the trap center prior to a first reorientation event. Although cells appear to swim away from each other, the observed radial cell spreading is a consequence of the ballistic nature of the cells immediately after release. In this regime, it is possible to estimate average speed as a measure of motility by analyzing many individual cell trajectories. Figure 2 and Movie S1 show the ballistic swimming behavior of 13 CC-125 cells for t = 0.75 s after release from the central pressure well. Confinement facilitates determination of average MSD (and thus U) by tracing individual cell trajectories, but this approach still remains time-consuming and laborious.

For ballistic swimmers, acoustic trap-and-release enables an alternate method to determine swimming speed from the variation in the polar moment of inertia, ΔJ, of a population of spreading cells. Brightfield video microscopy was used to record the spread of cell aggregates for 1–3 s (depending on cell type). Frames were converted into binary images, and ΔJ was calculated as a function of spreading time for an object representing the region occupied by cells (indicated by black pixels in binary images of cell distributions). The insets in Fig. 2b show representative binary images for ballistic spread of CC-125 cells. The ratio of ΔJ to the cross-sectional area (CSA) of the cell collective, ΔJ/CSA, is then used in place of MSD to automatically calculate U without needing to trace individual trajectories.

ΔJ/CSA Closely Approximates MSD for Radial Cell Spreading

The mean squared displacement of a collection of spreading cells is expressed as

$$\text{MSD} = \langle |\boldsymbol{x} - \boldsymbol{x_o}|^2 \rangle = \frac{1}{N}\sum_{n=1}^{N} |\boldsymbol{x_n} - \boldsymbol{x_{no}}|^2, \quad (3)$$

where $\boldsymbol{x} = \boldsymbol{x_n}$ is the location of cell n at time t, $\boldsymbol{x_o} = \boldsymbol{x_{no}}$ is the initial location of the cell, and N is the total number of cells in the trap. To determine the ratio ΔJ/CSA we first calculate the polar moment of inertia, $\tilde{J}$, for the composite region of spreading cells with respect to a centroidal coordinate system at time t as

$$\tilde{J} = I_{min} + I_{max} = \int r^2 dA, \quad (4)$$

where I_{min} and I_{max} are the principal second moments of area of the region, and r is the distance from an area element to the centroid: $r = |\boldsymbol{x} - \boldsymbol{x_c}|$. Next, the parallel axis theorem is used to account for the drift of the centroid if spreading is not perfectly axisymmetric. The total polar moment of inertia, J, with respect to the initial centroid of the cell collective at t = 0, is thus

$$J = \tilde{J} + d^2\text{CSA} = \tilde{J} + d^2 \int dA, \quad (5)$$

where CSA is the cross-sectional area at the current time, t, and d is the distance between the current centroid and the centroid at t = 0: $d = |\boldsymbol{x_c} - \boldsymbol{x_{co}}|$. Finally, to account for the finite initial radius of the cell cluster, the J value at t = 0, J_o, is subtracted from J to obtain the change in polar moment of inertia, ΔJ, defined as

$$\Delta J = J - J_o. \quad (6)$$

For a collection of uniform, discrete cells, each with cross-sectional area A_{cell}, $\tilde{J}$ becomes

$$\tilde{J} = \sum_{n=1}^{N} |\boldsymbol{x_n} - \boldsymbol{x_c}|^2 A_{cell}, \quad (7)$$

If spreading is perfectly axisymmetric the centroid of the spreading cells does not move, so $\boldsymbol{x_c} = \boldsymbol{x_{co}}$. Also, in a perfect acoustic trap, all cells are initially confined to the trap center,

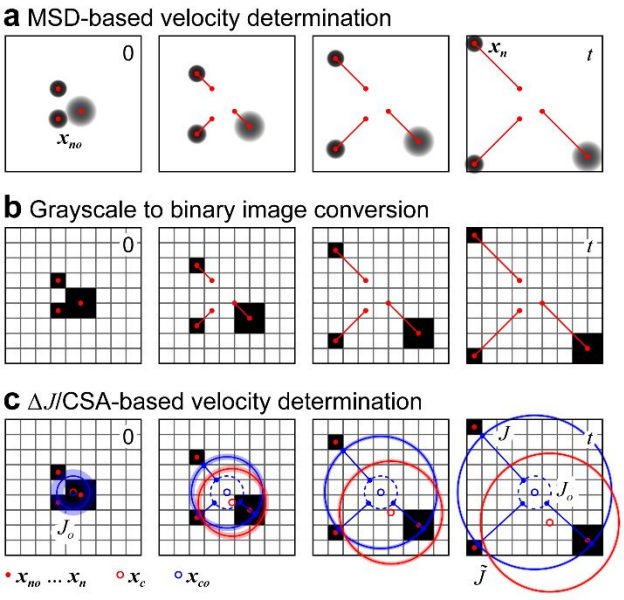

Fig. 4. Comparison of MSD- and ΔJ/CSA-based velocity determination. (a) Three randomly positioned cells move ballistically outward from their initial positions in the acoustic trap (note that this figure depicts representative simulated cells and not actual grayscale images of spreading cells). (b) Grayscale images are converted to binary images for ΔJ/CSA determination. (c) ΔJ is the difference between the polar area moment of inertia of the spreading cells at time t to that of the cell collective at t = 0 (both with respect to the initial object centroid). Here, ΔJ is illustrated by the difference between the solid blue (J) and dashed blue rings (J_o).

and $\boldsymbol{x_{no}} = \boldsymbol{x_{co}}$. Under these ideal conditions it can be shown (see Electronic Supplementary Information) that

$$\frac{\Delta J}{\text{CSA}} = \text{MSD} = \frac{1}{N}\sum_{n=1}^{N}|\boldsymbol{x_n} - \boldsymbol{x_{no}}|^2. \quad (8)$$

The effect of deviation from these idealizations is illustrated in Fig. 4. Randomly positioned cells (two in sharp focus and one slightly out of focus) move radially outward from an initially tight agglomerate (Fig. 4a). MSD is the average of the square of the red line lengths (the cell trajectories) from initial cell positions ($\boldsymbol{x_{no}}$) to those at time t ($\boldsymbol{x_n}$). After binary conversion of each image in the sequence, I_{min} and I_{max} are automatically computed using the ImageJ plugin BoneJ[39] to determine $\tilde{J}$. The evolution of $\tilde{J}$ is depicted in Fig. 4c by annular red rings of identical polar moment of inertia to the collection of cells. The parallel axis theorem is used to compute the polar moment of inertia, J, with respect to the centroid at t = 0. The resultant J is depicted by annular blue rings in Fig. 4c. Finally, ΔJ/CSA is the average of the square of the blue line lengths between rings representing J and J_o (dashed blue ring). Fig. 4 illustrates that the lengths of red lines representing the cell trajectories (square root of MSD) and blue lines representing the variation in the square root of ΔJ/CSA are nearly the same, but not identical owing to the imperfect trap, differences in cells size, and drift.

Although Eq. 8 is only strictly true for ideal trap-and-release conditions, empirically ΔJ/CSA is found to closely approximate MSD if the initial cell agglomerate is tightly packed, and if cells are highly uniform in size and small relative to the extent of

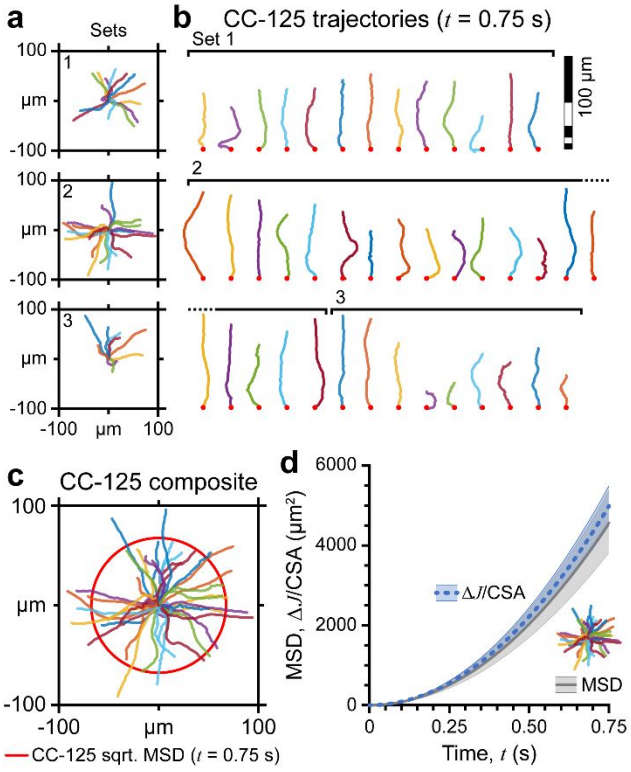

Fig. 5. Wild-type (CC-125) *C. reinhardtii* motility assessment. (a),(b) Plots of radial cell spreading and reoriented individual trajectories for three low-population release experiments. The duration of spreading shown in the plots corresponds to the ballistic swimming regime (t = 0.75 s). (c) Composite plot of cell spreading for all experiments. The extent of spread at t = 0.75 s is indicated by the solid red circle. (d) Comparison of U^2t^2 as functions of calculated MSD- and ΔJ/CSA-based speeds. Curve fits and s.d. bands are weighted by contributing sample sizes ($N_{CC\text{-}125}$ = 3, $n_{g,CC\text{-}125}$ = 13, 20, 9).

spreading. Here, we show that speeds experimentally-determined using MSD and ΔJ/CSA are almost equivalent. To allow tracing of individual cell trajectories, low numbers (~10) of trapped cells were used. Even so, the initially tight grouping of cells confounded automatic tracing, and trajectories were manually traced. Figure 5a-c shows individual and composite CC-125 trajectories for three release experiments. Cells swim radially away from the trap center, and reoriented trajectories (Fig. 5b) confirm ballistic behavior for the initial 0.75 s. A speed of 90±8 μm/s was calculated by fitting MSD = U^2t^2 to the measured MSD from 42 individual CC-125 trajectories. Binary imaging data were used to fit ΔJ/CSA = U^2t^2 yielding a speed of 94±5 μm/s. Figure 5d compares expressions U^2t^2 as functions of the two calculated speeds, demonstrating that ΔJ/CSA closely approximates MSD.

Mutant *C. reinhardtii* Cells Deviate Only Slightly from Ballistic Swimming Behavior

To establish the utility of acoustic trap-and-release, we applied the method to mutant *C. reinhardtii* cells with different swimming behaviors (Figs. 6 and 7). With diminished swimming speeds, mutant cells require more time to disperse from the initial aggregate. Inhibited swimming complicated even manual

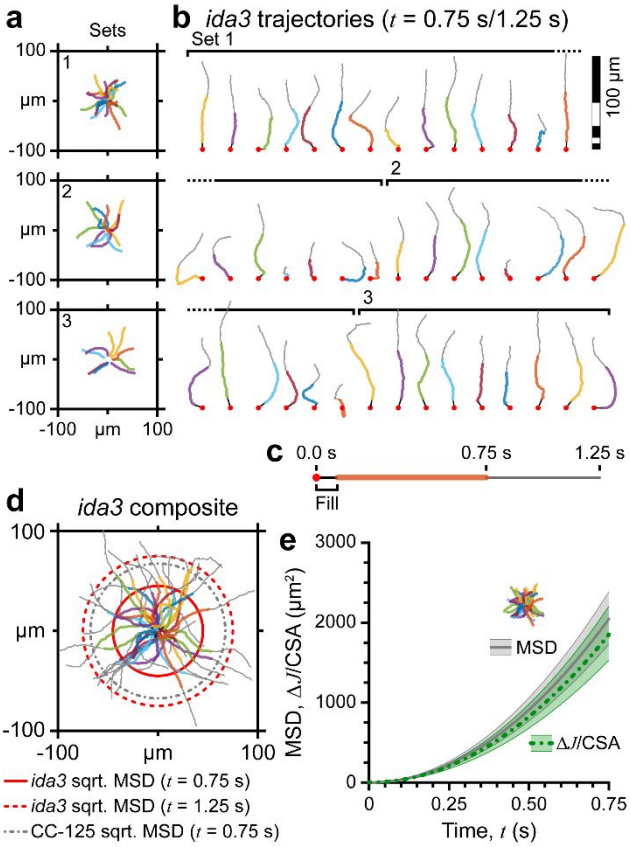

Fig. 6. Mutant *ida3* motility assessment. (a),(b) Plots of radial cell spreading and reoriented individual trajectories for three low-population *ida3* release experiments. The duration of spreading shown in the plots corresponds to the CC-125 ballistic swimming regime (t = 0.75 s). (c) Individual trajectories comprise three segments: *i*. a "fill" segment before manual tracing is possible, *ii*. a colored (thicker) segment corresponding to the CC-125 ballistic swimming regime, and *iii*. a gray segment from 0.75 s to the end of the ballistic period for *ida3* (t = 1.25 s). (d) Composite radial spread plot of trajectories that include the entire *ida3* ballistic swimming regime. Solid and dotted red circles indicate the extent of spread at 0.75 and 1.25 s, respectively. The dash-dot gray circle indicates the extent of spread of CC-125 at t = 0.75 s for reference. (e) Comparison of U^2t^2 as functions of calculated MSD- and ΔJ/CSA-based speeds for *ida3*. Curve fits and s.d. bands are weighted by contributing sample sizes (N_{ida3} = 3, $n_{g,ida3}$ = 21, 14, 9).

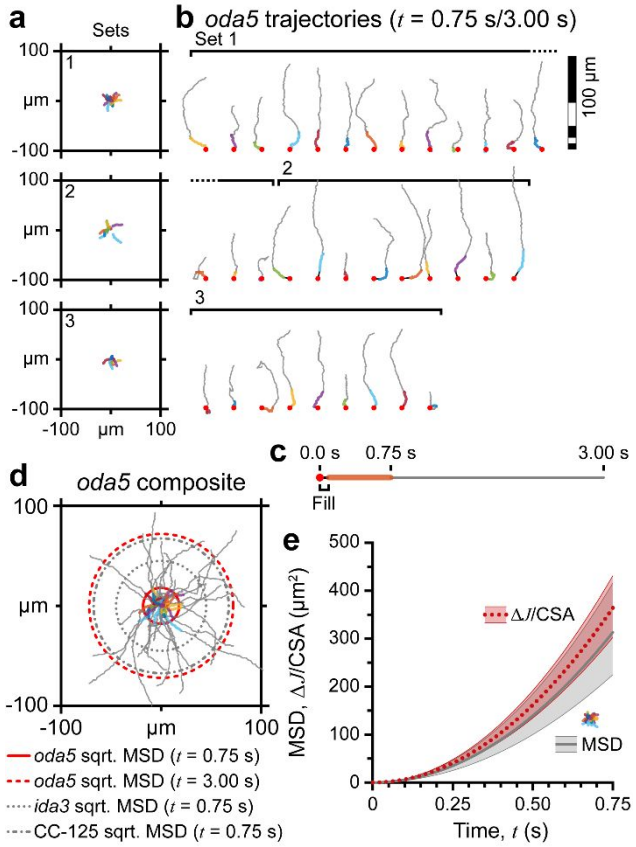

Fig. 7. Mutant *oda5* motility assessment. (a),(b) Plots of radial cell spreading and reoriented individual trajectories for three low-population *oda5* release experiments. The duration of spreading shown in the plots corresponds to the CC-125 ballistic swimming regime (t = 0.75 s). (c) Individual trajectories comprise three segments: *i*. a "fill" segment before manual tracing is possible, *ii*. a colored (thicker) segment corresponding to the CC-125 ballistic swimming regime, and *iii*. a gray segment from 0.75 s to the end of the ballistic period for *oda5* (t = 3.00 s). (d) Composite radial spread plot of trajectories that include the entire *oda5* ballistic swimming regime. Solid and dotted red circles indicate the extent of spread at 0.75 and 3.00 s, respectively. The dash-dot and dotted gray circles indicate the extent of spread of CC-125 and *ida3*, respectively, at t = 0.75 s for reference. (e) Comparison of U^2t^2 as functions of calculated MSD- and ΔJ/CSA-based speeds for *oda5*. Curve fits and s.d. bands are weighted by contributing sample sizes (N_{oda5} = 3, $n_{g,oda5}$ = 16, 9, 9).

tracing of cell trajectories during the initial 0.05–0.2 s after release. For *ida3* and *oda5*, mean squared displacement (MSD)-based speeds were determined using initial and final traced positions. For MSD-based estimates, the known time from release and the velocity at the initial traced position were used to fill in the missing segment for visual representation (see segment labelled "fill" in Figs. 6c and 7c). The filled-in segment did not affect calculated speeds; the MSD calculation does not include the fill segment and the calculation of the ratio ΔJ/CSA naturally incorporates the initial time without adjustment. Colored (thicker) segments are traced cell trajectories from the fill point up to t = 0.75 s to illustrate the distance travelled by the mutants during the ballistic period of the wild-type CC-125 cells (Figs. 6a-d and 7a-d). Terminal gray segments are traced trajectories from 0.75 s to the end of the ballistic period for *ida3* and *oda5*, 1.25 and 3.00 s, respectively.

Figure 6a,b,d shows individual and composite *ida3* trajectories for three low-number release experiments. Reoriented trajectories display ballistic swimming for ~1.25 s, maintaining similar verticality to the CC-125 trajectories at 0.75 s (Figs. 5b and 6b). Lacking the I1 dynein complex, the *ida3* mutant travels a shorter distance in a given time than CC-125 [see dash-dot gray (CC-125) and solid red (*ida3*) circles in Fig. 6d]; however, the distance travelled during the ballistic regime is approximately the same for the two organisms [see dash-dot gray (CC-125) and dashed red (*ida3*) circles in Fig. 6d]. This suggests that the mutation affects only swimming speed (i.e., distance travelled over time) but does not alter the

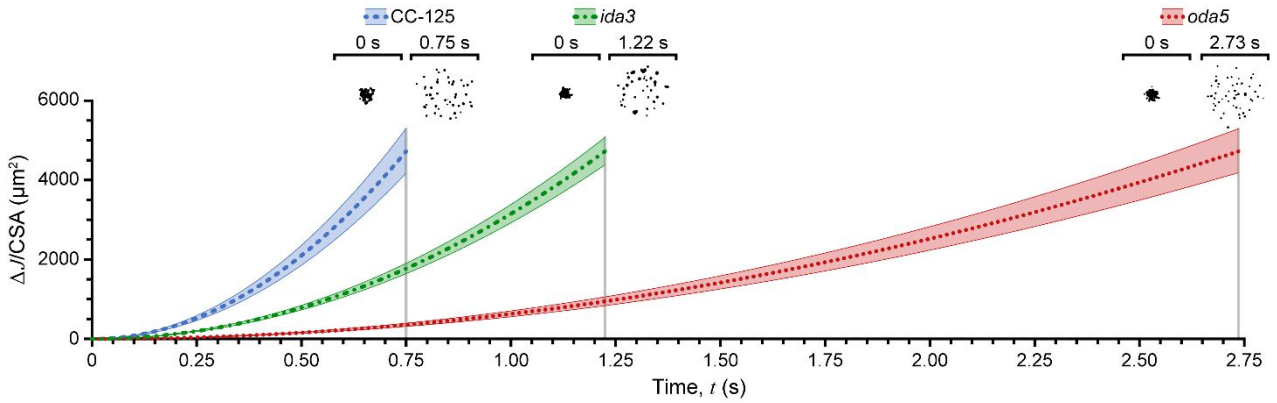

Fig. 8. Motility-based discrimination of wild-type (CC-125) *C. reinhardtii* and two mutants (*ida3* and *oda5*). Mutants exhibit impaired motility due to targeted defects of the flagella (lack of I1-dynein complex, *ida3*; lack of outer dynein arms, *oda5*). Spread duration for each cell type reflects the time to reach ΔJ/CSA equivalent to CC-125 at t = 0.75 s. Initial and final binary images suggest that cell distributions are similar for the three cell types.

distance to reorientation. The *ida3* speeds corresponding to the ballistic regime (t = 1.25 s) are 60±5 and 57±5 μm/s determined from MSD and ΔJ/CSA, respectively (Fig. 6e).

Similar plots are provided in Fig. 7 for *oda5* with a ballistic period of approximately 3 s. The *oda5* mutant, which lacks outer dynein arms, exhibits a lower beat frequency and a partial reversal of motion during the recovery stroke (i.e., cells appear to "stutter step"). Both behaviors contribute to severely inhibited swimming and the diminished net distance travelled [see dash-dot gray (CC-125), dotted gray (*ida3*), and solid red (*oda5*) circles in Fig. 7d]. Further, the more oscillatory body motion also appears to introduce tortuosity that promotes deviation from ballistic swimming (Fig. 7b). These local departures from ideal behavior are largely rectified at longer times (swimming is considered ballistic for ~3 s). Since the *oda5* beat frequency (previously reported as ~20–30 Hz;[7] unpublished measurement of current *oda5* beat frequency is ~20 Hz) is lower than the frame rate of the camera (38.15 fps), *oda5* trajectories were down sampled by a factor of two for clearer visualization. Again, MSD and ΔJ/CSA yield comparable speeds of 24±4 and 25±2 μm/s, respectively (Fig. 7e).

Acoustic Trap-and-Release Enables Rapid Motility Assessment

Having confirmed that ΔJ/CSA closely approximates MSD, we demonstrate acoustic trap-and-release to determine the motility of populations with a larger number of cells. Our method requires that the densely-packed cells at the center of the agglomerate can spread freely after release without being impeded by cells initially at the periphery of the pressure well. This prescribed a maximal capacity of the trap of ~50 cells. Confinement, release, and analysis of each experimental condition took a matter of seconds. Calculation of ΔJ was insensitive to phenomena that confound MSD determination (e.g., intersecting trajectories and out of focus cells). In addition, larger populations reduced the occurrence of skew. For repeat experiments, the microfluidic chamber was flushed and loaded with a new sample, enabling analysis of several hundreds of cells in a few minutes.

Figure 8 and Movie S2 show summary results with binary images illustrating the similarity in observed spreading over the course of the ballistic regime for each of the three cell types. Calculated speeds based on six repeat experiments are 92±5, 56±2, and 25±1 μm/s for CC-125, *ida3*, and *oda5*, respectively, almost identical to the low-population measurements. For reference, conventional speeds defined as total distance travelled over time are 94±22, 69±18, and 29±7 μm/s for CC-125, *ida3*, and *oda5* based on the individual trajectories of Figs. 5, 6 and 7.

Conclusions

An acoustic trap-and-release method was used to compare the motility of wild-type cells (strain CC-125) and two mutants [strains *ida3* (CC-2668) and *oda5* (CC-2236)]. Because swimming speed reflects flagellar function, a method capable of distinguishing these cells based solely on swimming metrics simplifies classification of such mutants, among other potential applications. Here, expected motility differences were clearly observed and quantified.

The expression for the primary acoustic radiation force (Eq. 1) reveals that multiple factors can affect the capacity of the acoustic trap. Regarding particle size, we note that the size discrepancy among the three cell types (which yields an approximately 36% reduction in the force applied to the slightly smaller *ida3* mutants) is unimportant as long as the trap strength is sufficient to create similarly sized aggregates for all cell types. Temperature control is not critical for device operation (i.e., to maintain consistent field parameters as in typical acoustic microfluidic device studies) but is necessary to ensure that chamber conditions do not approach the thermotolerance threshold for *C. reinhardtii* cells. Of more significance is confirmation that the acoustic trap-and-release does not adversely alter flagellar function or cell viability. Cell motility, as determined by spread speed, was invariant for five trap-and-release cycles performed on the same cell populations, which substantiates previous reports of the biocompatibility of acoustic-based cell manipulation.[48-51]

In water, the acoustic wavelength is ~1.5 mm at a frequency of 1 MHz, yielding a wavelength-to-chamber depth

ratio much greater than 10:1. Thus, the standing acoustic field varies minimally with vertical position, and chamber depth plays only a minor role in determining the device operating point. Chamber depth is, however, relevant to the spreading dynamics and subsequent analysis. A depth of 5–10X the cell diameter allowed for cell overlap during release (limiting collision-based reorientations) while providing vertical boundaries that promoted radial spread. In addition, the depth of 60 μm maintained sufficient optical focus to prevent spreading cells from swimming vertically out of the field of view. Because ΔJ/CSA is normalized by cross-sectional area, results are unaffected by apparent expansion due to defocus of the cells. Nonetheless, a small number of cells were observed to move in and out of focus over the course of a release experiment. Vertical (up or down) motion produces small deviations from purely radial swimming, which could contribute to a slight reduction in calculated speeds.

Acoustic confinement facilitates population-based analyses that accurately reproduce motility measures obtained (laboriously) by analyzing individual cells. The method is robust and even permits characterization of swimmers that deviate from ballistic behavior, which is assumed in the simple U^2t^2 swimming model. Although the calculated swimming metric (i.e., speed based on net distance travelled over time) is lower than the speed reported in the literature[7, 9, 15, 24-26] (here, the total distance travelled over time, e.g., ~92 μm/s versus ~94 μm/s for wild-type *C. reinhardtii*), the decrease is common to all three cell types. As expected, the less ballistic swimmers (*ida3* and *oda5*) deviate slightly more than the ballistic CC-125 cells. Thus, if the goal is to differentiate cells based on swimming efficiency, the acoustic trap-and-release is a compelling alternative to particle tracing. Accuracy could be improved by decreasing the microfluidic channel height to ~30 μm to further inhibit vertical swimming (see above).

Beyond general motility assessment, the temperature-controlled acoustic trap-and-release described here is also suited to investigate thermal effects on cells, including mammalian cells at or above a physiologically relevant temperature of 37°C. The applications of this approach include rapid assessment of spermatozoa motility or high-throughput screening of chemicals and other factors that might affect cilia/flagella function.

Conflicts of interest

There are no conflicts to declare.

Acknowledgements

This work was supported by the National Science Foundation under Grant No. CMMI-1633971. MK was also partially supported by the Spencer T. and Ann W. Olin Fellowship for Women in Graduate Study.

Notes and references

1. G. J. Pazour, N. Agrin, B. L. Walker and G. B. Witman, *J. Med. Genet.*, 2006, **43**, 62-73.
2. S. T. Christensen, L. B. Pedersen, L. Schneider and P. Satir, *Traffic*, 2007, **8**, 97-109.
3. M. A. Zariwala, M. R. Knowles and H. Omran, *Annu. Rev. Physiol.*, 2007, **69**, 423-450.
4. M. Fliegauf, T. Benzing and H. Omran, *Nat. Rev. Mol. Cell Biol.*, 2007, **8**, 880-893.
5. W. F. Marshall, *J. Cell Biol.*, 2008, **180**, 17-21.
6. S. K. Dutcher, B. Huang and D. J. L. Luck, *J. Cell Biol.*, 1984, **98**, 229-236.
7. C. J. Brokaw and R. Kamiya, *Cell Motil. Cytoskeleton*, 1987, **8**, 68-75.
8. P. V. Bayly, B. L. Lewis, P. S. Kemp, R. B. Pless and S. K. Dutcher, *Cytoskeleton*, 2010, **67**, 56-69.
9. P. V. Bayly, B. L. Lewis, E. C. Ranz, R. J. Okamoto, R. B. Pless and S. K. Dutcher, *Biophys. J.*, 2011, **100**, 2716-2725.
10. R. Bower, D. Tritschler, K. VanderWaal, C. A. Perrone, J. Mueller, L. Fox, W. S. Sale and M. E. Porter, *Mol. Biol. Cell*, 2013, **24**, 1134-1152.
11. E. L. Hunter, K. Lechtreck, G. Fu, J. Hwang, H. W. Lin, A. Gokhale, L. M. Alford, B. Lewis, R. Yamamoto, R. Kamiya, F. Yang, D. Nicastro, S. K. Dutcher, M. Wirschell and W. S. Sale, *Mol. Biol. Cell*, 2018, **29**, 886-896.
12. F. Yang, J. Pavlik, L. Fox, C. Scarbrough, W. S. Sale, J. H. Sisson and M. Wirschell, *Am. J. Physiol.-Lung Cell. Mol. Physiol.*, 2015, **308**, L569-L576.
13. J. M. Brown, M. Mosley, D. Montes-Berrueta, Y. Q. Hou, F. Yang, C. Scarbrough, G. B. Witman and M. Wirschell, *PLoS One*, 2017, **12**, 14.
14. V. F. Geyer, F. Julicher, J. Howard and B. M. Friedrich, *Proc. Natl. Acad. Sci. USA*, 2013, **110**, 18058-18063.
15. B. Qin, A. Gopinath, J. Yang, J. P. Gollub and P. E. Arratia, *Sci. Rep.*, 2015, **5**, 9190.
16. B. F. L. Edwards, R. J. Wheeler, A. R. Barker, F. F. Moreira-Leite, K. Gull and J. D. Sunter, *Proc. Natl. Acad. Sci. USA*, 2018, **115**, E7341-E7350.
17. N. Ueki and K. Wakabayashi, *Proc. Natl. Acad. Sci. USA*, 2018, **115**, E1061-E1068.
18. W. F. Marshall, *J. Biomol. Screening*, 2009, **14**, 133-141.
19. C. D. Silflow and P. A. Lefebvre, *Plant Physiol.*, 2001, **127**, 1500-1507.
20. G. Pennarun, E. Escudier, C. Chapelin, A. M. Bridoux, V. Cacheux, G. Roger, A. Clement, M. Goossens, S. Amselem and B. Duriez, *Am. J. Hum. Genet.*, 1999, **65**, 1508-1519.
21. G. J. Pazour, *Curr. Biol.*, 2004, **14**, R575-R577.
22. N. Hornef, H. Olbrich, J. Horvath, M. A. Zariwala, M. Fliegauf, N. T. Loges, J. Wildhaber, P. G. Noone, M. Kennedy, S. E. Antonarakis, J. L. Blouin, L. Bartoloni, T. Nusslein, P. Ahrens, M. Griese, H. Kuhl, R. Sudbrak, M. R. Knowles, R. Reinhardt and H. Omran, *Am. J. Respir. Crit. Care Med.*, 2006, **174**, 120-126.
23. D. Antony, A. Becker-Heck, M. A. Zariwala, M. Schmidts, A. Onoufriadis, M. Forouhan, R. Wilson, T. Taylor-Cox, A. Dewar, C. Jackson, P. Goggin, N. T. Loges, H. Olbrich, M. Jaspers, M. Jorissen, M. W. Leigh, W. E. Wolf, M. L. A. Daniels, P. G. Noone, T. W. Ferkol, S. D. Sagel, M. Rosenfeld, A. Rutman, A. Dixit, C. O'Callaghan, J. S. Lucas, C. Hogg, P. J. Scambler, R. D. Emes, E. M. K. Chung, A. Shoemark, M. R. Knowles, H. Omran, H. M. Mitchison and Uk10K, *Hum. Mutat.*, 2013, **34**, 462-472.
24. R. Kamiya, *Cell Motil. Cytoskeleton*, 1995, **32**, 98-102.

25. J. S. Guasto, K. A. Johnson and J. P. Gollub, *Phys. Rev. Lett.*, 2010, **105**, 168102.
26. H. Kurtuldu, D. Tam, A. E. Hosoi, K. A. Johnson and J. P. Gollub, *Phys. Rev. E*, 2013, **88**, 013015.
27. COMSOL Inc., COMSOL Multiphysics 5.2a, 2016.
28. M. Cui, M. M. Binkley, H. N. Shekhani, M. Y. Berezin and J. M. Meacham, *Biomicrofluidics*, 2018, **12**, 034110.
29. P. B. Allen and D. T. Chiu, *Anal. Chem.*, 2008, **80**, 7153-7157.
30. A. Neild, S. Oberti and J. Dual, *Sens. Actuators, B*, 2007, **121**, 452-461.
31. F. Garofalo, T. Laurell and H. Bruus, *Phys. Rev. Appl.*, 2017, **7**, 054026.
32. A. Nilsson, F. Petersson, H. Jonsson and T. Laurell, *Lab Chip*, 2004, **4**, 131-135.
33. M. Evander, A. Lenshof, T. Laurell and J. Nilsson, *Anal. Chem.*, 2008, **80**, 5178-5185.
34. S. K. Dutcher, *Methods Cell Biol.,* 1995, **47**, 531-540.
35. J. A. Holmes and S. K. Dutcher, *J. Cell Sci.*, 1989, **94**, 273-285.
36. R. Sager and S. Granick, *Ann. N. Y. Acad. Sci.*, 1953, **56**, 831-838.
37. B. Xie, S. Bishop, D. Stessman, D. Wright, M. H. Spalding and L. J. Halverson, *ISME J.*, 2013, **7**, 1544-1555.
38. J. Schindelin, I. Arganda-Carreras, E. Frise, V. Kaynig, M. Longair, T. Pietzsch, S. Preibisch, C. Rueden, S. Saalfeld, B. Schmid, J. Y. Tinevez, D. J. White, V. Hartenstein, K. Eliceiri, P. Tomancak and A. Cardona, *Nat. Methods*, 2012, **9**, 676-682.
39. M. Doube, M. M. Kłosowski, I. Arganda-Carreras, F. P. Cordelières, R. P. Dougherty, J. S. Jackson, B. Schmid, J. R. Hutchinson and S. J. Shefelbine, *Bone*, 2010, **47**, 1076-1079.
40. The MathWorks Inc., MATLAB r2017b, 2017.
41. R. Barnkob, P. Augustsson, T. Laurell and H. Bruus, *Phys. Rev. E*, 2012, **86**, 056307.
42. P. B. Muller, R. Barnkob, M. J. H. Jensen and H. Bruus, *Lab Chip*, 2012, **12**, 4617-4627.
43. T. Laurell, F. Petersson and A. Nilsson, *Chem. Soc. Rev.*, 2007, **36**, 492-506.
44. O. Manneberg, B. Vanherberghen, J. Svennebring, H. M. Hertz, B. Onfelt and M. Wiklund, *Appli. Phys. Lett.*, 2008, **93**, 063901.
45. D. J. Collins, B. Morahan, J. Garcia-Bustos, C. Doerig, M. Plebanski and A. Neild, *Nat. Comm.*, 2015, **6**, 9686.
46. F. Guo, Z. M. Mao, Y. C. Chen, Z. W. Xie, J. P. Lata, P. Li, L. Q. Ren, J. Y. Liu, J. Yang, M. Dao, S. Suresh and T. J. Huang, *Proc. Natl. Acad. Sci. USA*, 2016, **113**, 1522-1527.
47. P. Augustsson, J. T. Karlsen, H. W. Su, H. Bruus and J. Voldman, *Nat. Comm.*, 2016, **7**, 11556.
48. J. Hultstrom, O. Manneberg, K. Dopf, H. M. Hertz, H. Brismar and M. Wiklund, *Ultrasound Med. Biol.*, 2007, **33**, 145-151.
49. J. J. Shi, D. Ahmed, X. Mao, S. C. S. Lin, A. Lawit and T. J. Huang, *Lab Chip*, 2009, **9**, 2890-2895.
50. B. Vanherberghen, O. Manneberg, A. Christakou, T. Frisk, M. Ohlin, H. M. Hertz, B. Onfelt and M. Wiklund, *Lab Chip*, 2010, **10**, 2727-2732.
51. P. Li, Z. M. Mao, Z. L. Peng, L. L. Zhou, Y. C. Chen, P. H. Huang, C. I. Truica, J. J. Drabick, W. S. El-Deiry, M. Dao, S. Suresh and T. J. Huang, *Proc. Natl. Acad. Sci. USA*, 2015, **112**, 4970-4975.
52. J. Friend and L. Y. Yeo, *Rev. Mod. Phys.*, 2011, **83**, 647-704.
53. M. Settnes and H. Bruus, *Phys. Rev. E*, 2012, **85**, 016327.
54. F. Petersson, A. Nilsson, C. Holm, H. Jonsson and T. Laurell, *Lab Chip*, 2005, **5**, 20-22.
55. A. Lenshof, C. Magnusson and T. Laurell, *Lab Chip*, 2012, **12**, 1210-1223.
56. K. Yosioka and Y. Kawasima, *Acta Acust. Acust.*, 1955, **5**, 167-173.
57. L. P. Gorkov, *Dokl. Akad. Nauk SSSR*, 1961, **140**, 88-91.
58. H. Bruus, *Lab Chip*, 2012, **12**, 1014-1021.
59. P. Glynne-Jones, C. E. M. Demore, C. W. Ye, Y. Q. Qiu, S. Cochran and M. Hill, *IEEE Trans. Ultrason. Ferroelectr. Freq. Control*, 2012, **59**, 1258-1266.
60. P. Glynne-Jones and M. Hill, *Lab Chip*, 2013, **13**, 1003-1010.
61. S. Rafai, L. Jibuti and P. Peyla, *Phys. Rev. Lett.*, 2010, **104**, 098102.
62. M. Garcia, S. Berti, P. Peyla and S. Rafai, *Phys. Rev. E*, 2011, **83**, 035301.
63. J. R. Howse, R. A. L. Jones, A. J. Ryan, T. Gough, R. Vafabakhsh and R. Golestanian, *Phys. Rev. Lett.*, 2007, **99**, 048102.

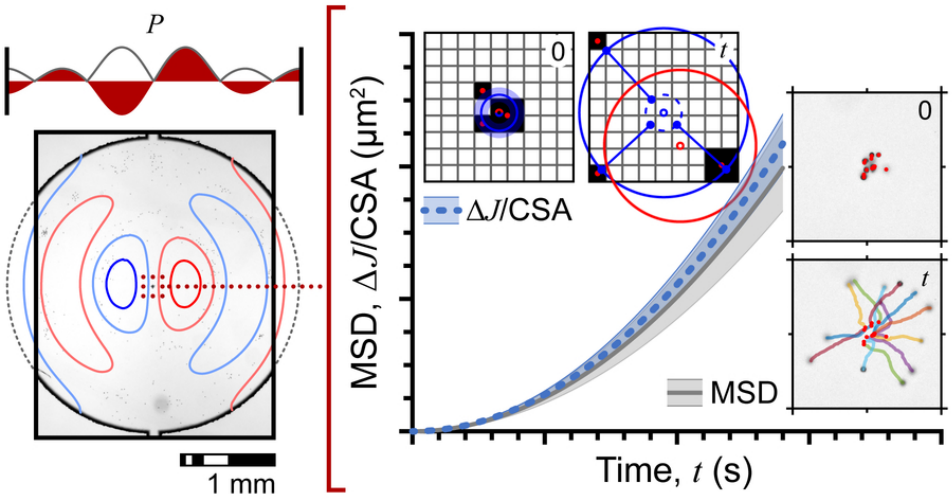

80x40mm (300 x 300 DPI)